Acta Oceanol. Sin., 2024, Vol. 43, No. 5, P. 1–15
https://doi.org/10.1007/s13131-024-2317-8
http://www.aosocean.com
E-mail: ocean2@hyxb.org.cn

Spatiotemporal characteristics of water exchange between the Andaman Sea and the Bay of Bengal

Yihao Wang[1, 2, 3], Feng Zhou[1, 2, 3*], Xueming Zhu[4*], Ruijie Ye[2, 3], Yingyu Peng[2, 3, 5], Zhentao Hu[2, 3], Haoran Tian[2, 3], Na Li[6]

[1] Ocean College, Zhejiang University, Zhoushan 316021, China

[2] State Key Laboratory of Satellite Ocean Environment Dynamics, Second Institute of Oceanography, Ministry of Natural Resources, Hangzhou 310012, China

[3] Observation and Research Station of Yangtze River Delta Marine Ecosystems, Ministry of Natural Resources, Zhoushan 316022, China

[4] Southern Marine Science and Engineering Guangdong Laboratory (Zhuhai), Zhuhai 519080, China

[5] School of Oceanography, Shanghai Jiao Tong University, Shanghai 200240, China

[6] School of Marine Sciences, Sun Yat-sen University, Zhuhai 519080, China

Received 5 January 2024; accepted 12 March 2024

Abstract

A high-resolution customized numerical model is used to analyze the water transport in the three major water passages between the Andaman Sea (AS) and the Bay of Bengal, i.e., the Preparis Channel (PC), the Ten Degree Channel (TDC), and the Great Channel (GC), based on the daily averaged simulation results ranging from 2010 to 2019. Spectral analysis and Empirical Orthogonal Function (EOF) methods are employed to investigate the spatiotemporal variability of the water exchange and controlling mechanisms. The results of model simulation indicate that the net average transports of the PC and GC, as well as their linear trend, are opposite to that of the TDC. This indicates that the PC and the GC are the main inflow channels of the AS, while the TDC is the main outflow channel of the AS. The transport variability is most pronounced at surface levels and between 100 m and 200 m depth, likely affected by monsoons and circulation. A 182.4-d semiannual variability is consistently seen in all three channels, which is also evident in their second principal components. Based on sea level anomalies and EOF analysis results, this is primarily due to equatorial winds during the monsoon transition period, causing eastward movement of Kelvin waves along the AS coast, thereby affecting the spatiotemporal characteristics of the flow in the AS. The first EOF of the PC flow field section shows a split at 100 m deep, likely due to topography. The first EOF of the TDC flow field section is steady but has potent seasonal oscillations in its time series. Meanwhile, the first EOF of the GC flow field section indicates a stable surface inflow, probably influenced by the equatorial Indian Ocean's eastward current.

Key words: Andaman Sea, water exchange, Regional Ocean Modeling Systems (ROMS), Kelvin waves, spatiotemporal characteristics

Citation: Wang Yihao, Zhou Feng, Zhu Xueming, Ye Ruijie, Peng Yingyu, Hu Zhentao, Tian Haoran, Li Na. 2024. Spatiotemporal characteristics of water exchange between the Andaman Sea and the Bay of Bengal. Acta Oceanologica Sinica, 43(5): 1–15, doi: 10.1007/s13131-024-2317-8

1 Introduction

The Andaman Sea (AS) spans 670 000 km^2 in the northeastern tropical Indian Ocean. It's bounded by Myanmar, Thailand, Malaysia, and the Andaman and Nicobar Islands. Resulting from the collision between the Indian and Eurasian plates, the AS has varied depths and intricate seafloor topography, including the AS basin with depths exceeding 1 800 m. The Bay of Bengal (BOB), encompassing 2.17 × 10^6 km^2 in the northern Indian Ocean, averages 2 586 m in depth.

The AS connects to the BOB via three main channels on its west (Fig. 1): The shallow Preparis Channel (PC) at about 400 m deep, the Ten Degree Channel (TDC) nearing 1 000 m deep, and the Great Channel (GC) at approximately 1 800 m deep.

Since the AS below 1 800 m is an isolated oceanic basin, these channels are crucial for water exchange, which is essential for climate and deep circulation (Wang et al., 2014; Huang et al., 2020; Liao et al., 2020; Zhou et al., 2022). The water exchange is regulated by the monsoon circulation and atmospheric events. The AS and the BOB are influenced by monsoon winds, with northeasterly winds prevailing in the winter and southwesterly winds in the summer. During the northeast monsoon, a cyclonic circulation is formed in the BOB, which can later transition to a basin-scale anticyclonic circulation as the monsoon progresses (Varkey et al., 1996; Eigenheer and Quadfasel, 2000; Somayajulu et al., 2003). This changing circulation pattern could lead to seasonal variability in water exchange. In addition to the monsoon influence, this region also periodically experiences intense convective

Foundation item: The Joint Advanced Marine and Ecological Studies (JAMES) in the Bay of Bengal and eastern equatorial Indian Ocean supported by the Global Change and Air-Sea Interaction II Program under contract Nos GASI-01-EIND-STwin and GASI-04-WLHY-03; Zhejiang Provincial Ten Thousand Talents Plan under contract No. 2020R52038.
*Corresponding author, E-mail: zhoufeng@sio.org.cn; zhuxueming@sml-zhuhai.cn

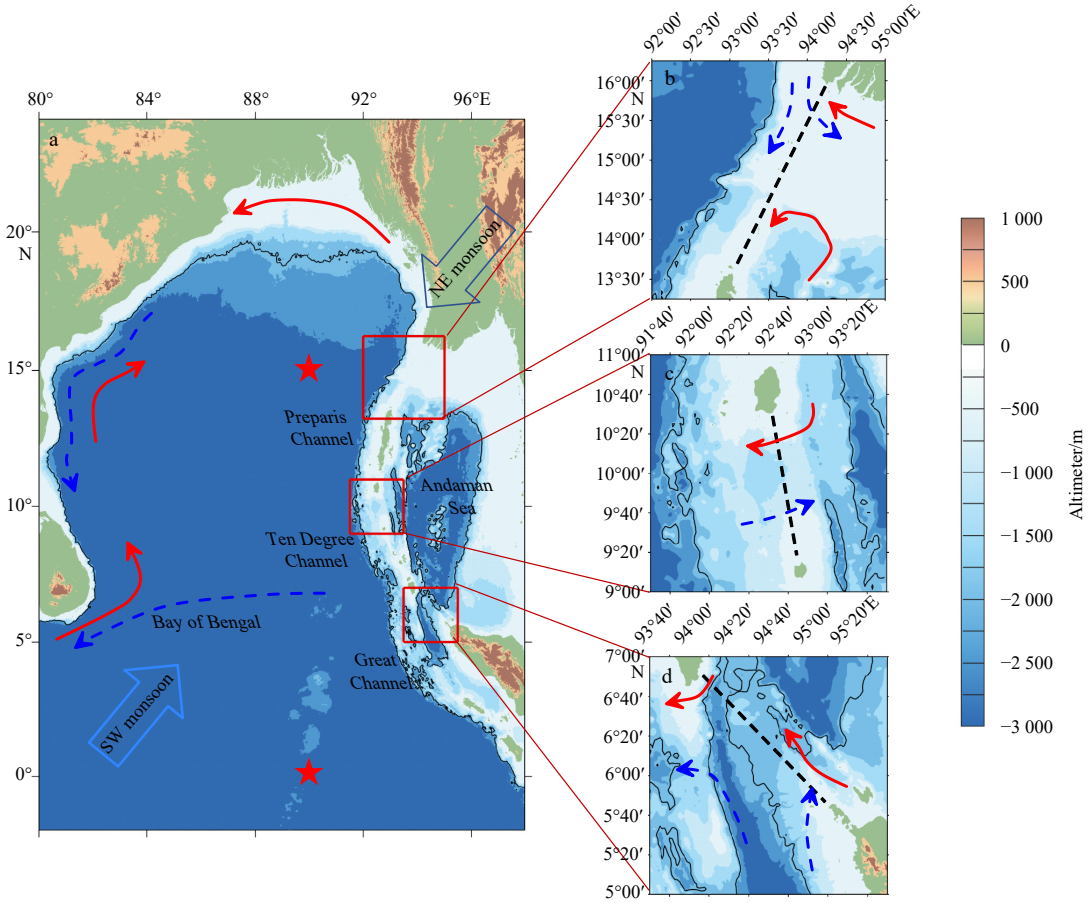

Fig. 1. Altimeter of Bay of Bengal (a) and three major passages (b, c, and d). The black solid line represents the 1 800-m isobath, the black dashed lines indicate the three sections used for transport analysis, two red stars mark the mooring sites, the red solid arrows and the blue dashed arrows represent the sea surface circulation patterns during the southwest (SW) monsoon and the northeast (NE) monsoon, respectively.

activities and rainfall events. The Madden-Julian Oscillation (MJO) is a significant contributor to the tropical atmospheric intraseasonal variability in the Indian Ocean (Zhang, 2005; Vialard et al., 2009; Yoneyama et al., 2013; Roman-Stork et al., 2020), which also affects the variability of ocean currents (Girishkumar et al., 2011; Krishnamurti et al., 2017; Trott and Subrahmanyam, 2019; Chen and Wang, 2021).

A distinct feature that sets the AS apart from other similar regions is the impact of equatorial Kelvin waves. During the monsoon, the vertical propagation of equatorial zonal wind energy in the Indian Ocean affects the flow field, resulting in the eastward propagation of semiannual Kelvin waves. Some Kelvin waves are reflected as Rossby waves at the eastern boundary near Sumatra, and mooring data shows that there is a significant variability in deep ocean currents at 90°E, suggesting that high-frequency signals can reach deep into the ocean bottom and influence the mixing and exchange of deep waters (Amol et al., 2022; Ye et al., 2023b). Other Kelvin waves travel along the coastline, entering the AS via the GC and affecting the variability of surface currents along its eastern boundary (McPhaden, 1982; Sengupta et al., 2001; Iskandar and McPhaden, 2011; Huang et al., 2018). Prior studies have shown that sea level anomalies along the Andaman coast experience semiannual changes, primarily due to the influence of equatorial zonal winds that generate Kelvin waves (McCreary et al., 1993; Clarke and Liu, 1993; Chen, 2022).

Unfortunately, the lack of long-term and deep ocean current data in the AS and BOB has led to research focusing mainly on the surface circulation within the AS (Cheng et al., 2017; Liao et al., 2020; Zhou et al., 2022), with less understanding of the temporal and spatial variations in water exchange. Moreover, due to the complex factors influencing the currents in the AS, the primary drivers of these variations are not well understood. It is essential to analyze the long-term transport and the characteristics of their variations through these channels and to discuss the modulation mechanisms.

As a part of the "Joint Advanced Marine and Ecological Studies (JAMES)" in the BOB and eastern equatorial Indian Ocean, this research delves into the spatiotemporal dynamics and governing mechanisms of water exchange transports in the AS and BOB. We utilized the Regional Ocean Modeling System (ROMS) model, focusing on daily variables like velocity and sea surface height ranging from 2010 to 2019. Initially, we analyzed the transports in three AS channels, advancing to a deeper spatiotemporal analysis. Subsequently, using Empirical Orthogonal Function (EOF) and spectral examination, we explored their modulation mechanisms. Structurally, the paper is organized as follows: Section 2 details the data sources; Section 3 compares and validates model outcomes with observational data; Section 4 delves into a model-based analysis; Section 5 offers discussion and summary.

2 Data and methods

2.1 *Numerical model*

This study uses the output from a customized ROMS (Shche-

petkin and McWilliams, 2005) for the northern Indian Ocean. The ROMS domain covers 34°S–28°N, 26°–150°E. The simulation extends from January 2010 to December 2019. The horizontal grid resolution of the model is (1/24)°, and the vertical is divided into 30 layers using the terrain-following coordinate. The bathymetric data is obtained from the combination results of the General Bathymetric Chart of Oceans (GEBCO_08) global bathymetric database (0.5′ × 0.5′). The minimum water depth of the model is set to be 5 m, and the maximum depth uses the actual value from GEBCO_08.

The surface atmospheric forcing field data used is the Climate Forecast System Reanalysis (CFSR; Saha et al., 2010) data from the National Centers for Environmental Prediction (NCEP), which have the temporal resolution of 6 h and horizontal resolution of about 0.2°–0.3°. This dataset has been widely used in global and coastal ocean numerical simulation (Mo et al., 2016; Shi et al., 2016). The sea surface atmospheric forcing field is calculated and provided by the bulk-formulas (Fairall et al., 2003). The lateral boundary conditions are obtained from interpolation of the simulation results of the Chinese Global Operational Oceanography Forecasting System (CGOFS). The water level boundary adopts the Chapman scheme, the two-dimensional velocity boundary adopts the Flather scheme, the three-dimensional velocity and temperature-salinity boundaries adopt the Radiation-Nudging hybrid scheme. The freshwater discharge from river run off is considered in the system, with a climatological monthly cycle. In addition, climatology nudging is turned off to better simulate the seasonal and interannual variation of temperature and salinity fields of the system. The Ensemble Optimal Interpolation (EnOI; Evensen, 2003) data assimilation method is used to optimize the model initial fields. More details of the model configuration can be found in the references of Kourafalou et al. (2015), Ji et al. (2015), and Zhu et al. (2022).

2.2 *Satellite data*

The satellite-based daily ocean surface velocities are attained from the Ocean Surface Current Analysis-Real Time (OSCAR) product, it is available beginning January 2010 with a horizontal resolution of (1/3)° × (1/3)° and 1-d intervals (Bonjean and Lagerloef, 2002; Johnson et al., 2007). It represents the total ocean current (both geostrophic and Ekman components) of the upper 30 m. This product has been shown to be reliable in the regime of the East India Coastal Current (Mukherjee et al., 2014) and West India Coastal Current (Amol et al., 2014).

In order to verify model's sea level anomalies (SLA), this study is conducted using SLA data from E.U. Copernicus Marine Service Information. The Sea Level Thematic Assembly Centre (SL-TAC) product provides altimeter satellite data which covers sea surface height anomalies from 2010 to 2019 and is estimated by Optimal Interpolation.

2.3 *Mooring data*

To validate the model's performance, this study utilizes data from two buoys of the Research Moored Array for African-Asian-Australian Monsoon Analysis and Prediction (RAMA; McPhaden et al., 2009). One buoy (15°N, 90°E) provided temperature and salinity data from 4 m to 140 m depth ranging from 2010 to 2019. The other buoy, positioned on the equator (0°, 90°E), supplied flow field data for comparison, covering depths from the sea surface to 350 m.

2.4 *Surface drifters*

Hydrographic surveys were carried out on board of R/V *Xiangyanghong 06* and R/V *Xiangyanghong 10* during an international cooperation cruise named JAMES. Two surface drifting buoys were deployed in the Great Channel on December 9, 2019. This deployment acquired real-time monitoring of surface ocean currents, which is valuable for verifying the reliability of real-time ocean current predictions and observations.

2.5 *Water transport calculation*

The sections in this document is determined by the line connecting the south and north coasts of the strait (Figs 1b, c, and d). Since transport is the result of the area and the velocity component perpendicular to that area, the phase angle θ of the section will not affect the final result of the transport. The velocity component perpendicular to its section is obtained from the model's meridional and zonal velocities and the phase angle of the section. The velocities need to be processed, and here we calculate the velocity perpendicular to the section, u_{cross} and the velocity along the section, u_{along} as follows:

$$\begin{cases} u_{\text{cross}} = u \cdot \sin\theta - v \cdot \cos\theta, \\ u_{\text{along}} = u \cdot \cos\theta + v \cdot \sin\theta, \end{cases} \tag{1}$$

$$T = \sum_{i=1}^{m} \sum_{j=1}^{n} u_{\text{cross},ij} \cdot \Delta A_{ij}, \tag{2}$$

where T is the total transport of the section, the $u_{\text{cross},ij}$ is the velocity component perpendicular to the ij-th grid point. The ΔA_{ij} denotes the area element at the ij-th grid point. By accumulating the points on the grid, the channel water transport is calculated.

3 Model validation

As Fig. 2 shows, both model output and RAMA data is monthly averaged to obtain the climatological mean. The RAMA data shows that there are two peaks in surface temperature around March and September, which can also be shown by the ROMS. Furthermore, there is good agreement in the vertical structures of salinity and temperature between these two datasets. Overall, the vertical structures of temperature and salinity of ROMS and their seasonal variations are consistent with observations, which validate the reliability of the ROMS ocean state.

Due to the lack of long-term data for the Indian Ocean, we selected the RAMA dataset that includes data from 2010 to 2019 along the equator for comparison with current velocities (highlighted by red stars in Fig. 1). Figure 3 outlines monthly averages of meridional and zonal velocities from both the model and RAMA to generate climatological means. The zonal velocities (Figs 3a and b) display substantial congruence in magnitude and time-based variations, emphasizing a clear semiannual cycle. Despite slight variances in the numerical values of meridional velocities (Figs 3c and d), the contribution of the zonal flow velocity to the total flow is numerically more substantial, accounting for 77% in RAMA and 81% in ROMS, their distributional tendencies are largely parallel.

Overall, the vertical structure and seasonal variability of the flow field in ROMS align well with observations from the RAMA dataset, underscoring the reliability of the ROMS simulation in representing flow patterns.

To validate the ROMS surface circulation over the AS, long-term averaged seasonal features of surface currents in the ROMS are compared with the satellite-based OSCAR data (Fig. 4). Both two datasets show that the surface circulation in the AS exhibit

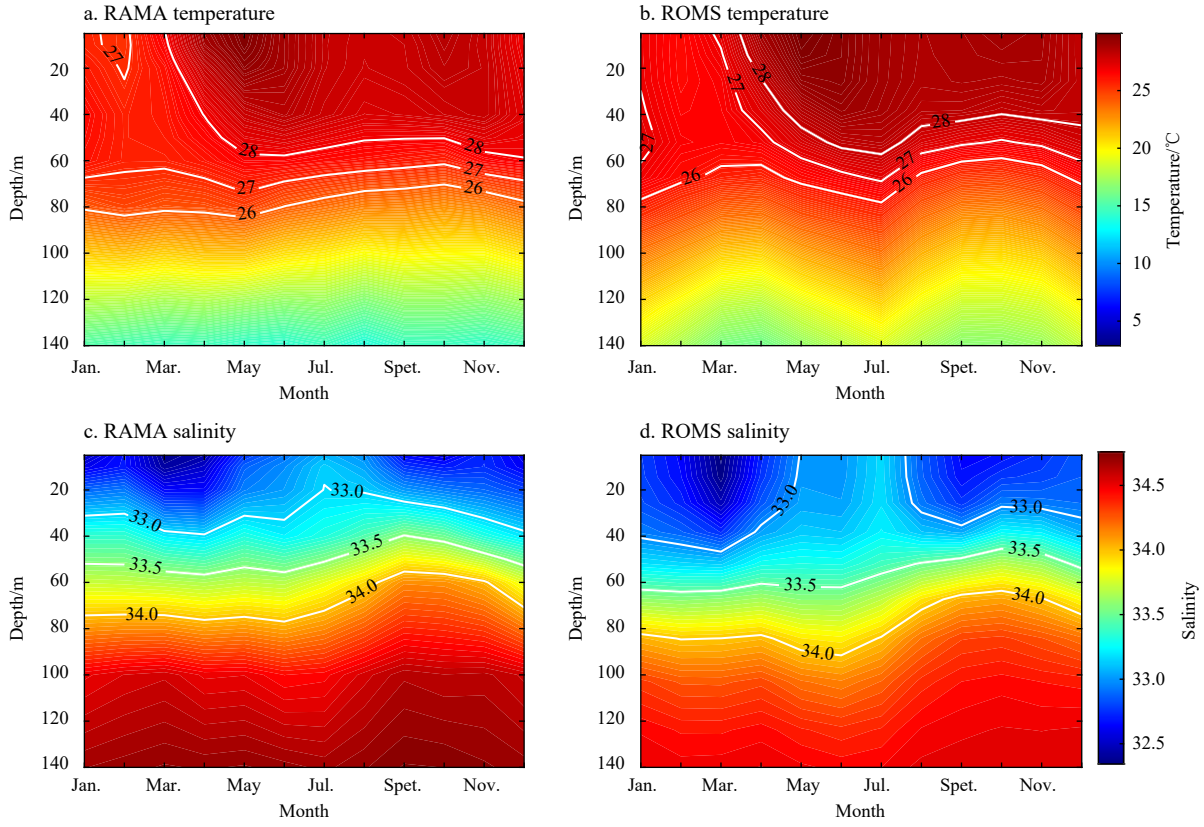

Fig. 2. The climatological monthly variability of temperature and salinity profiles averaged over the RAMA mooring (15°N, 90°E) during 2010–2019, based on RAMA (a and c) and ROMS (b and d). RAMA, Research Moored Array for African-Asian-Australian Monsoon Analysis and Prediction; ROMS, Regional Ocean Modeling System model.

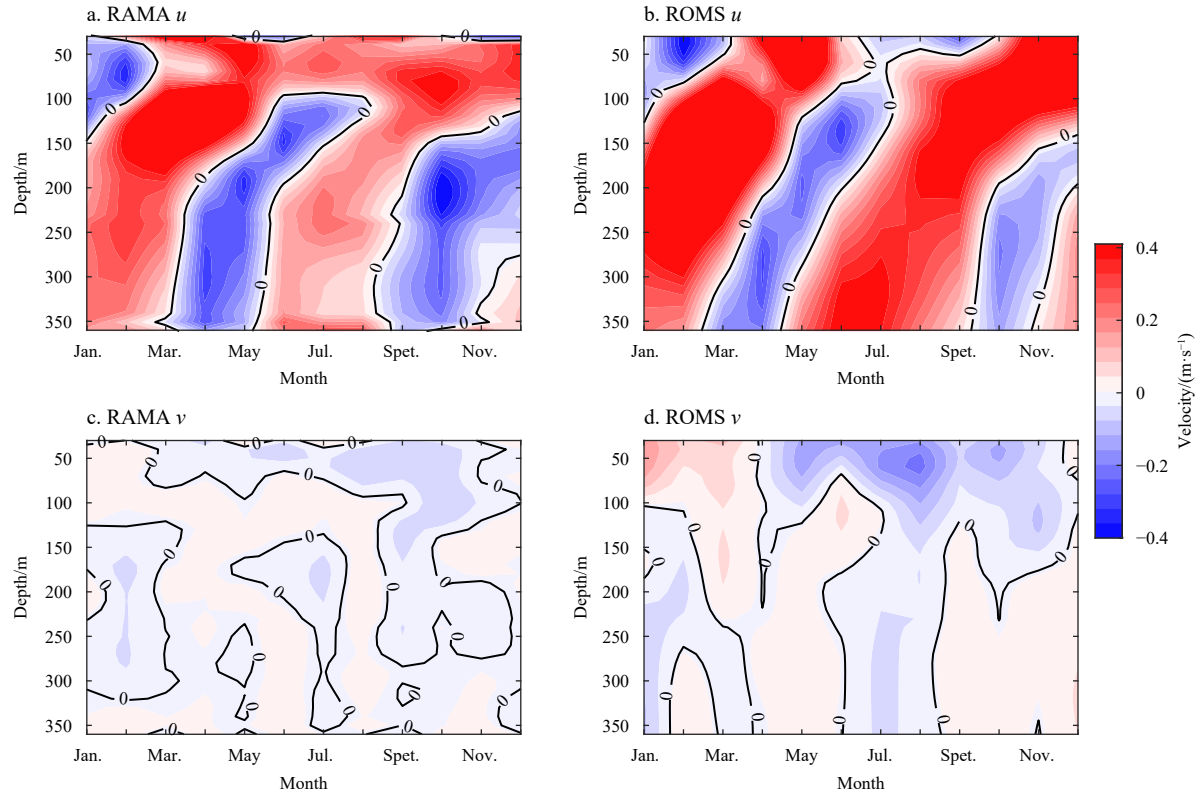

Fig. 3. The climatological monthly variability of zonal (u) and meridional (v) velocities profiles averaged over the RAMA mooring (0°, 90°E) during 2010–2019, based on RAMA (a and c) and ROMS (b and d). RAMA, Research Moored Array for African-Asian-Australian Monsoon Analysis and Prediction; ROMS, Regional Ocean Modeling System model.

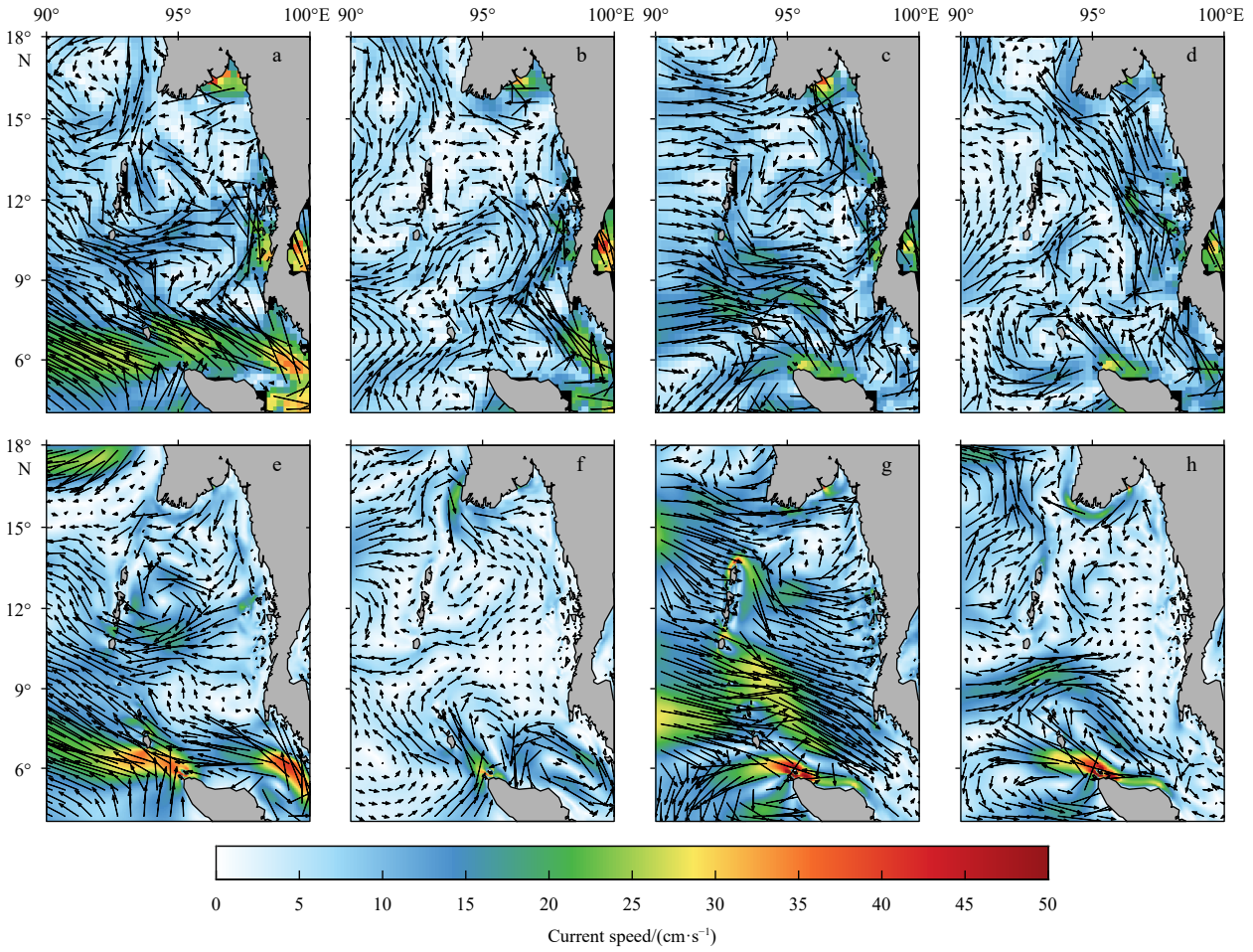

Fig. 4. The climatological seasonal surface flow (color shaded for current speed (cm/s), arrows for current direction) in winter (a, e), spring (b, f), summer (c, g), and autumn (d, h) in the Andaman Sea during 2010–2019, extracted from the OSCAR (a–d) data and ROMS (e–h), respectively. OSCAR, Ocean Surface Current Analysis-Real Time product; ROMS, Regional Ocean Modeling System model.

distinct seasonal variations. There is no gridded long-term *in-situ* current observation in this region, but the good agreement of surface circulation between the ROMS and the OSCAR across three channels proves the reliability of flows described by the ROMS.

An international cooperation cruise, named the JAMES, was conducted in the eastern equatorial Indian Ocean from December 2019 to February 2020, during which two surface drifters were released. Based on the trajectories of the drifters, we compared them to the average flow field from ROMS during the same period when the northeast monsoon was prevalent in the GC area and there were eddies at the channel entrance (Fig. 5). The observed drifter paths (moving clockwise from the GC towards the TDC) and the drifter velocities (indicated by arrow size) roughly corresponded to the ROMS flow field, indicating a certain level of reliability in velocity.

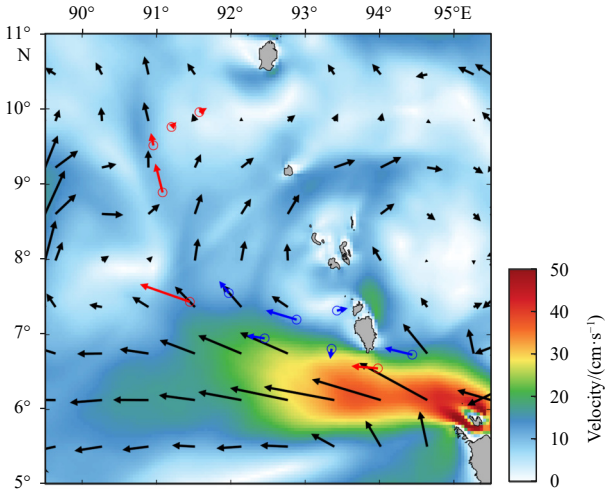

Fig. 5. Drifter trajectories within the ROMS flow field. The red and blue dots represent two drifter's trajectory points respectively, while the direction and size of the arrows indicate the drifter's flow direction and velocity. ROMS, Regional Ocean Modeling System model.

4 Results

4.1 *Water properties*

The nine sections shown in Fig. 6 are obtained by extracting the 10-year averaged temperature, salinity, and density data from the cross-sections represented in Fig. 1, specifically panels Fig. 1b, c, and d. Except for the PC, the minimum temperature in the water exchange sections of the AS is around 4℃, the maximum salinity is approximately 34.79, and the maximum density is around 1 033.7 kg/m^3. Comparing the different channels, it is evident that the temperature, salinity, and density contour lines for the PC (Figs 6a, d, and g) exhibit prominent protrusions. This phe-

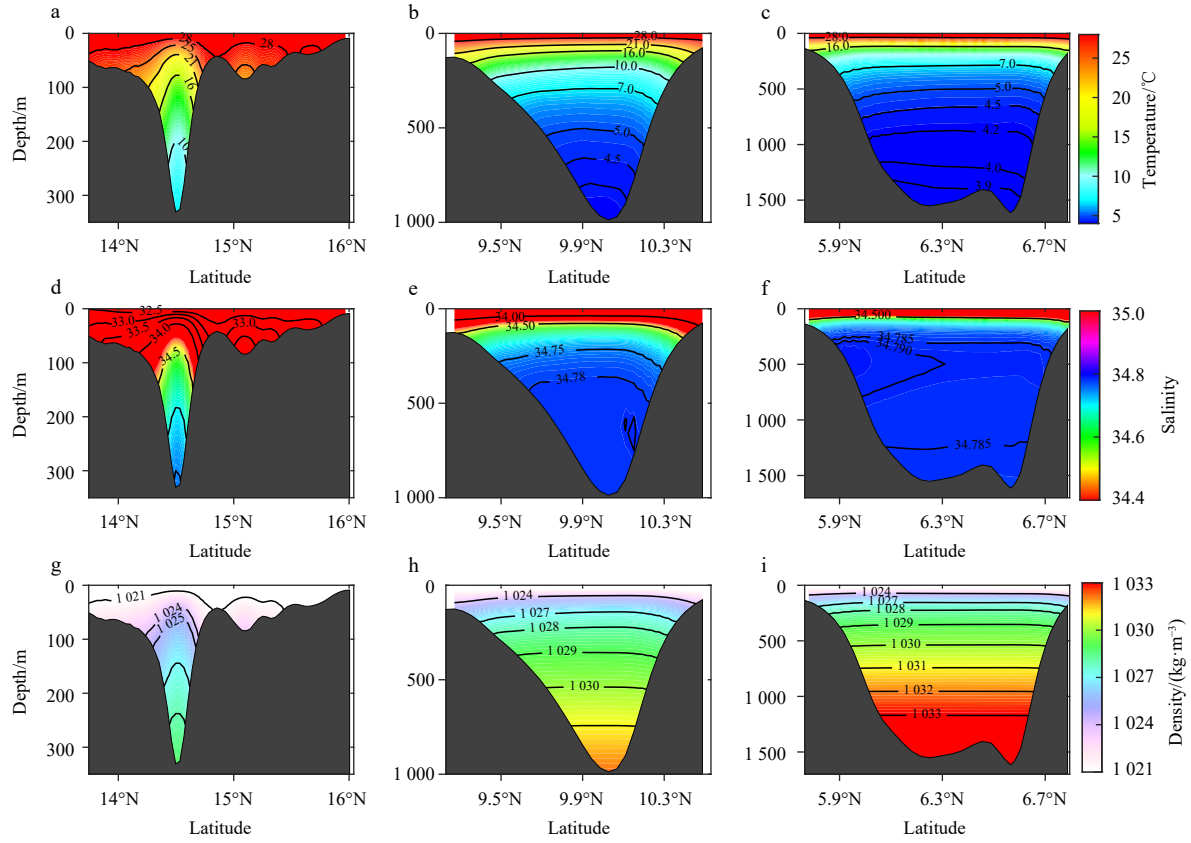

Fig. 6. Vertical sections of temperature (a, b, and c), salinity (d, e, and f), and density (g, h, and i) for the Preparis Channel , the Ten Degree Channel, and the Great Channel, respectively.

nomenon might arise from the hindrance imposed by the ridges on either side of the channel and the difference in seabed height between the AS and the BOB. Observational data also suggest the significance of the PC as a water exchange passage with distinct water properties on either side (Ye et al., 2023a; Lin et al., 2023). Additionally, the contour lines for temperature and density in the other two channels also exhibit protrusions, with some inclination near the coastal areas, possibly due to water exchange or coastal currents (Du et al., 2023).

Temperature and density sections in the TDC and the GC indicate relatively stable stratification. As for salinity, the TDC and the GC exhibit salinity cores around 10.2°N and 6°N, respectively, the GC also displaying a noticeable reversal in salinity gradients with a salinity core present along its southern coast. Moreover, the depths of these cores are quite close. Nonetheless, given the limitations of the model, verification through field observations is necessary to validate the salinity cores within the water exchange channels.

4.2 *Spatial variability*

Velocity sections (Figs 7a, b, and c) match the data from Figs 1b, c, and d, representing 10-year average velocities perpendicular to the sections towards the AS. The PC and the TDC sections display northward and southward flow cores, with southern cores being more pronounced. These channels show opposite flow directions, indicating stable flow cores. In contrast, the GC section exhibits multi-layer flow field, akin to the Luzon Strait (Cai et al., 2023). Above 600 m, it flows into the AS, while from 600 m to 1 500 m, it flows outward.

For transport calculations at consistent depths across the sections, we multiplied velocity with unit depth sectional area (Figs 7d, e, and f). It indicates seasonally varying flow field for the PC and the TDC sections, with the TDC being the key passage for continuous seasonal transport from the BOB to the AS around 200 m. The GC section shows consistent eastward surface transport.

In order to analyze their primary spatial and temporal variations, we applied an EOF decomposition on the 10-year cross section flow fields of the channels (Fig. 8).

EOF1 for the PC section is divided at 100 m depth, with the surface representing the wide shallow ocean, and below 100 m being the narrow deep passage (Fig. 8a). Previous observational research has indicated multi-layer water exchange within the PC (Ye et al., 2023a), suggesting that factors related to the seabed may influence the flow field up and down 100 m in the PC section. For the TDC section, EOF1 exhibits long-term inflow into the AS, and its first principal component displays strong seasonal variability, likely related to the Indian Ocean's intraseasonal oscillations dominated by the MJO (Figs 9b and h). The EOF1 of the GC section is relatively stable, with a strong surface component, possibly related to the Indian Ocean's robust eastward flow (Cheng et al., 2017; Huang et al., 2018).

There are commonalities among the modes of the three channels. The second mode, EOF2, of the PC, the TDC and the GC explains 25.76%, 19.94%, and 14.58% of their variances, respectively. According to the power spectra of their principal components (Fig. 9), we observed significant semiannual variability in all three channels (Figs 9g, h, and i). The semiannual variability in the Indian Ocean is likely dominated by the semiannual Kelvin waves. During the monsoon transition period, the propagation of

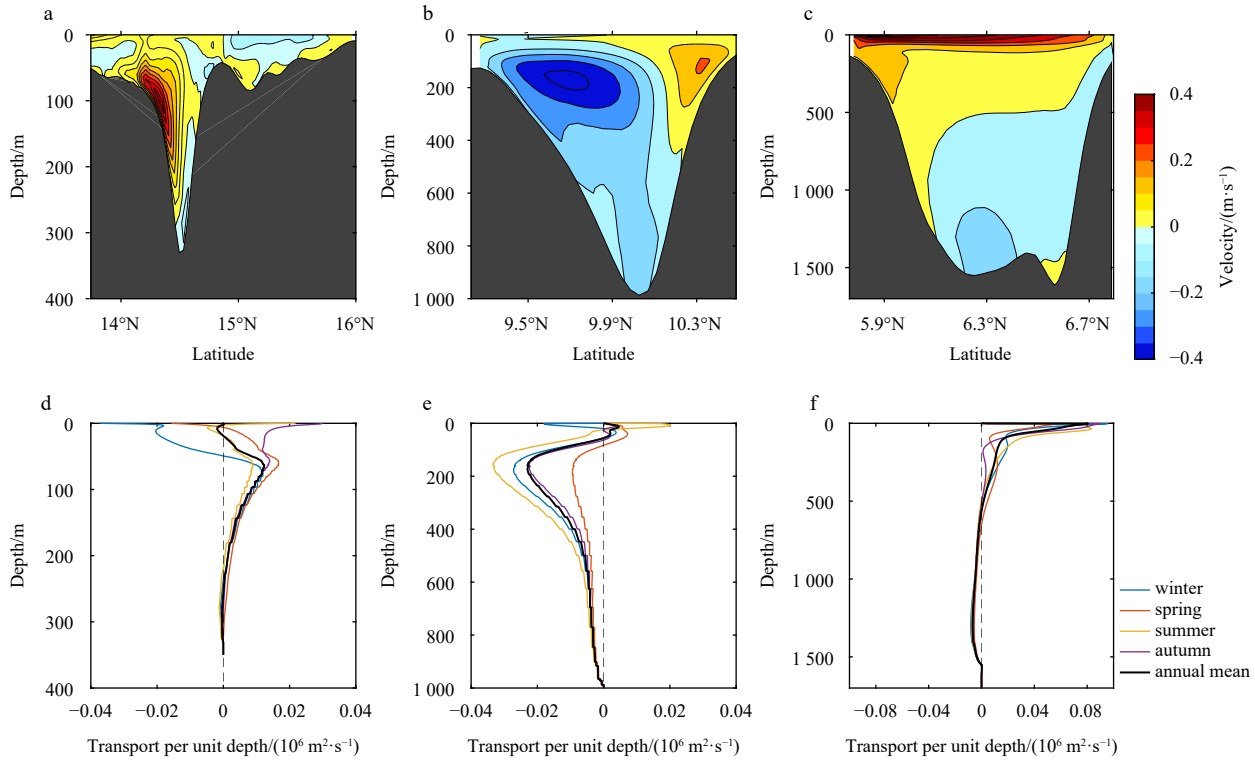

Fig. 7. Vertical sections and transport profiles for the Preparis Channel (a and d), the Ten Degree Channel (b and e) and the Great Channel (c and f). The positive value denotes the inflow from the Bay of Bengal to the Andaman Sea, while the negative value is opposite.

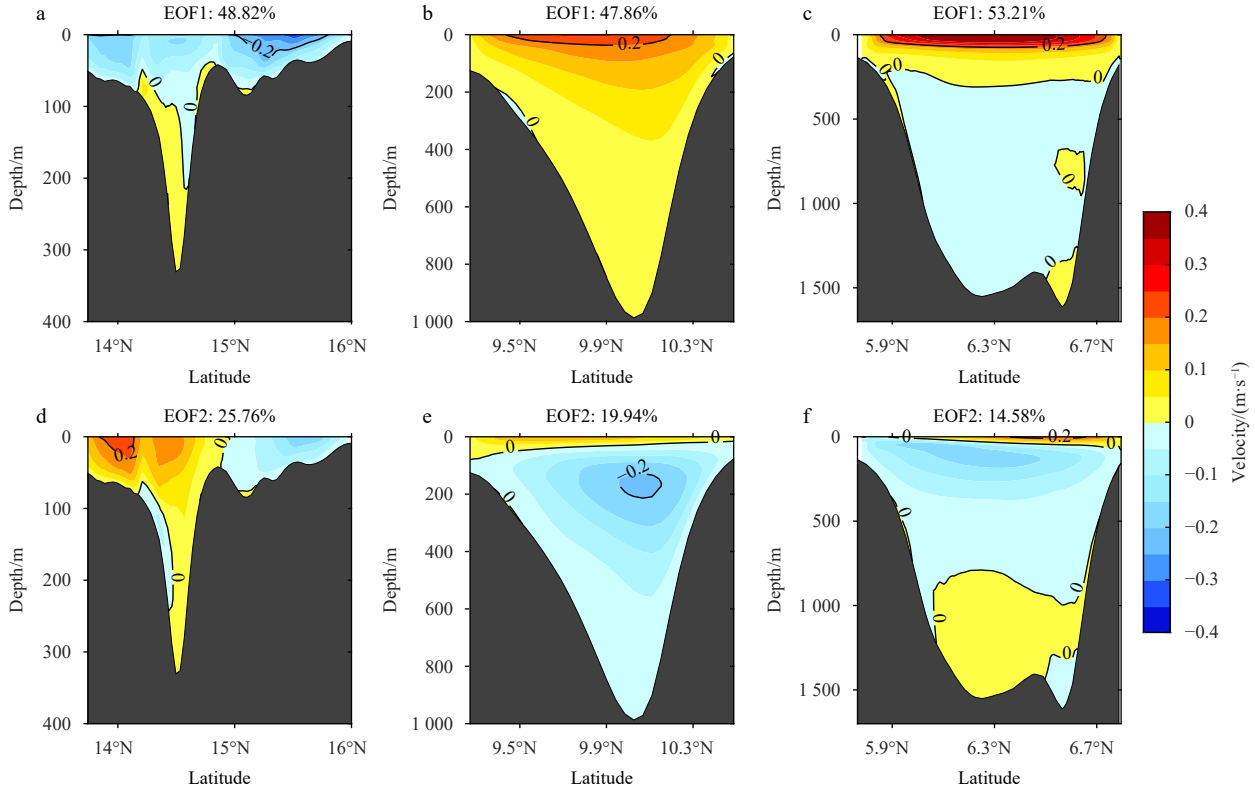

Fig. 8. The Empirical Orthogonal Function (EOF) modes for the Preparis Channel (a and d), the Ten Degree Channel (b and e), and the Great Channel (c and f).

Kelvin waves may influence the upper ocean (Chen, 2022). Specifically, for the PC section, EOF2 has a maximum core value at 15°N (Fig. 8d), with the northern core situated south of the Irrawaddy Delta, which is also the exit pathway of Kelvin waves in-

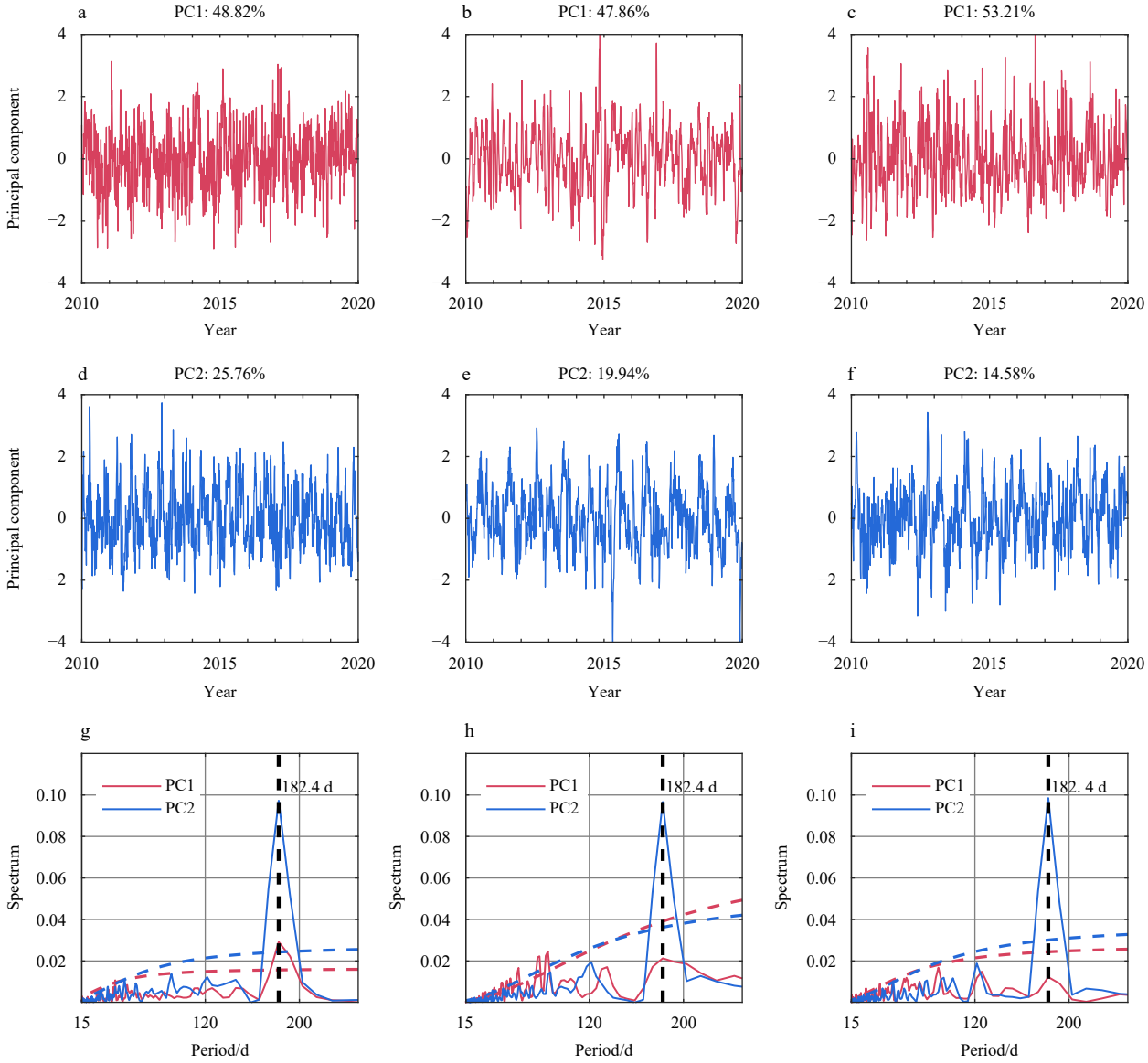

Fig. 9. The first principal component (PC1), the second principal component (PC2) time series and their power spectrum corresponding to the Preparis Channel (a, d, and g), the Ten Degree Channel (b, e, and h), and the Great Channel (c, f, and i). The red and blue lines indicates the 95% confidence interval.

to the AS. The southern core, located north of the Andaman Islands, is likely influenced by the island's coastal circulation (Chatterjee et al., 2017). The ten-year average net transports for the three channels are 1.14×10^6 m^3/s, -8.31×10^6 m^3/s, and 3.63×10^6 m^3/s for the PC, the TDC, and the GC, respectively (negative values represent westward transport, and positive values represent eastward transport). In addition to the three channels primarily studied in this paper, significant water exchange also occurs through the Strait of Malacca (0.12×10^6 m^3/s) and the smaller channels between these channels (add up to 0.28×10^6 m^3/s), as is shown in Fig. 10.

The analysis above demonstrates that all three channels share a strong semiannual variability in their flow fields, which may be associated with the remote influence of equatorial Kelvin waves. This aspect will be further investigated in the following sections.

4.3 *Temporal variability*

In order to better study the annual variation and the linear trends, a low-pass filter is applied to the full-depth transport data of three channel sections (Figs 1b, c, and d) in the ROMS from early January 2010 to the end of December 2019 (Fig. 11). The PC and the GC represent inflow channels, while the TDC represents an outflow channel. All three channels exhibit noticeable interannual periodic variations, and the significant fluctuations still persist after a 120-d filter, indicating the substantial contribution of periodic variations longer than 120 d to the temporal changes in transports (Fig. 11). This can also be observed in the subsequent spectral analysis plots (Fig. 12), where all three channels' power spectra share a semiannual cycle of approximately 182.4 d, which could be associated with the eastward Kelvin waves propagation instigated by the semiannual zonal wind shifts amid monsoon seasons in the equatorial Indian Ocean (Han et al., 2001; Sengupta et al., 2001, 2004; Iskandar and McPhaden, 2011; Huang et al., 2018; Zhang et al, 2021). The long-term linear trend of transport is also estimated using linear regression method, for the PC, the TDC, and the GC sections, the annual regression coefficient are -0.1×10^6 m^3/s, 0.22×10^6 m^3/s, and -0.13×10^6 m^3/s respectively (with positive values indicating an increasing aver-

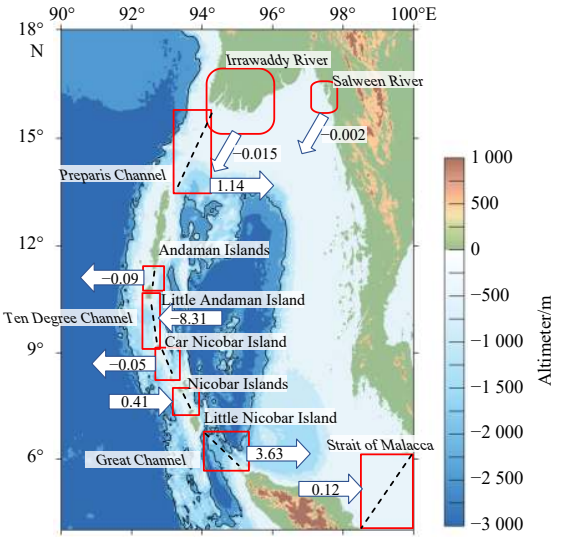

Fig. 10. Schematic of the transports through various channels in the Andaman Sea. The red straight-edged rectangles represent the exchange of seawater through the channels, the red rounded rectangles represent freshwater runoff input, and the black dashed lines represent the cross sections used for calculations. Negative values represent westward transport, and positive values represent eastward transport, with units in 10^6 m^3/s.

age transport). This suggests that the long-term transport trend in the TDC is contrary to the other two channels.

To understand the frequency composition of the three channels' transport variability, a spectral analysis is conducted. It indicates that strong intraseasonal variability is evident in all three channels (Fig. 12). Within the equatorial Indian Ocean, the MJO is recognized as a significant contributor to the tropical atmosphere's intraseasonal variability (Yoneyama et al., 2013). The MJO and the equatorial semiannual meridional winds influence atmospheric wind patterns, triggering active equatorial Kelvin and Rossby waves, which significantly affect the variability of the equatorial Indian Ocean's upper-ocean currents (Sengupta et al., 2007; Rao et al., 2010; Nagura and McPhaden, 2012; Webber et al., 2014; Pujiana and McPhaden, 2020).

To explore the relationship between monsoons and water transports, we examined the mean transport of the three channels in the AS during two monsoon periods (Fig. 13): the southwest monsoon (May–September) and the northeast monsoon (December–February). Notably, the two southern channels, the TDC and the GC, exhibit larger water transports during the southwest monsoon in most years compared to the northeast monsoon. This result may be attributed to the substantial precipitation during the southwest monsoon, which enhances water exchange in the Indian Ocean. However, this phenomenon is less pronounced in the PC, possibly due to its closer proximity to the continent, shallower water depths, and significant freshwater in-

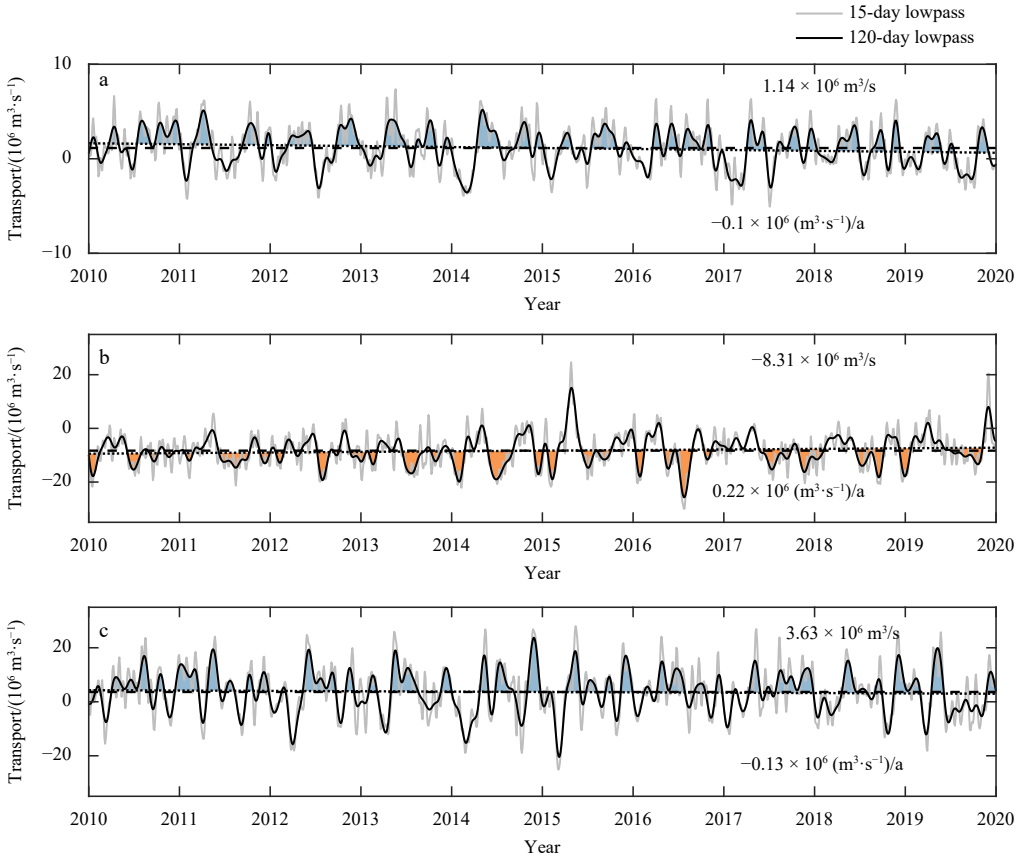

Fig. 11. Time series and trends of transport in the Preparis Channel (a), the Ten Degree Channel (b), and the Great Channel (c) based on Regional Ocean Modeling Systems model output. The dashed lines represent the average value of the channel transport, the dotted lines represent the linear trend of the channel transport, the thin gray lines and thick black lines indicate the 15-d low-passed filtered time series and 120-d low-passed filtered time series. Positive (negative) transport means that water flows into (out of) the Andaman Sea. The gray-blue shades indicate the inflow into the Andaman Sea, while the orange shades signify the outflow. The upper right of the graph is the average net transport, and the lower right is the regression coefficient of the transport.

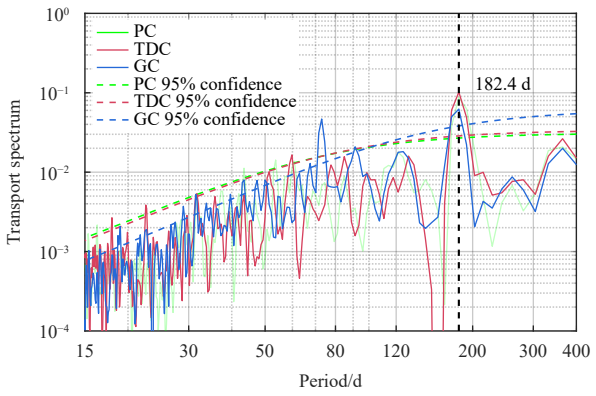

Fig. 12. Power spectra of full depth water transport in three channels based on unfiltered Regional Ocean Modeling Systems model data. The dashed green, red, and blue lines indicate the 95% confidence interval. PC, Preparis Channel; TDC, Ten Degree Channel; GC, Great Channel.

put from river like the Irrawaddy River (Pargaonkar and Vinayachandran, 2022).

To clearly illustrate the temporal variability of transports, we also provide the average transport and standard deviation for the three channels during winter, spring, summer, autumn, southwest monsoon period, northeast monsoon period, and annual periods (Table 1). The three channels exhibit the highest average transport during spring, which is also the southwest monsoon prevailing period. In terms of standard deviation, the PC and the GC have larger transport standard deviations compared to the TDC, indicating that the transport variations in the TDC are more stable.

4.4 *Influence of Kelvin waves*

Previous research has shown that during the seasonal reversal of the monsoon, equatorial zonal winds induce Kelvin waves that propagate eastward along the equatorial Indian Ocean, enter the AS along the coast of Sumatra, and finally exit the AS through the PC (Rao et al., 2010; Cheng et al., 2017). Kelvin waves lose energy when they encounter the coast and the remaining part propagates along the shoreline, so we select a coastal path at 100-m water depth from the equator at 90°E (referred to as EQ hereafter) to the GC, and then along the coast to the PC (Fig. 14a). In order to investigate the temporal variability of water transports among the three channels, we first verified the reliability of the model's SLA to explore the influence of equatorial Kelvin waves. We extracted SLA data from SL-TAC product and from the ROMS model for comparison (Figs 14b and c), which shows good agreement over the 10-year period, demonstrating the model's ability to accurately reflect the changes in sea surface height. Additionally, the periodic variations in sea surface height along this path can be observed (Figs 14b and c).

To further investigate the propagation relationship among them, we extracted the SLA time series for the EQ, GC, and PC (indicated by the red lines in Fig. 14). This allowed us to analyze their variations over a 10-year period (Fig. 15a). It can be observed that the EQ, GC, and PC exhibit highly similar waveforms with clear annual variations. These waveforms show some phase shifts among them. Further cross-correlation analysis (Figs 14b, c, and d) reveals that the GC lags the EQ by 9 d, the PC lags the

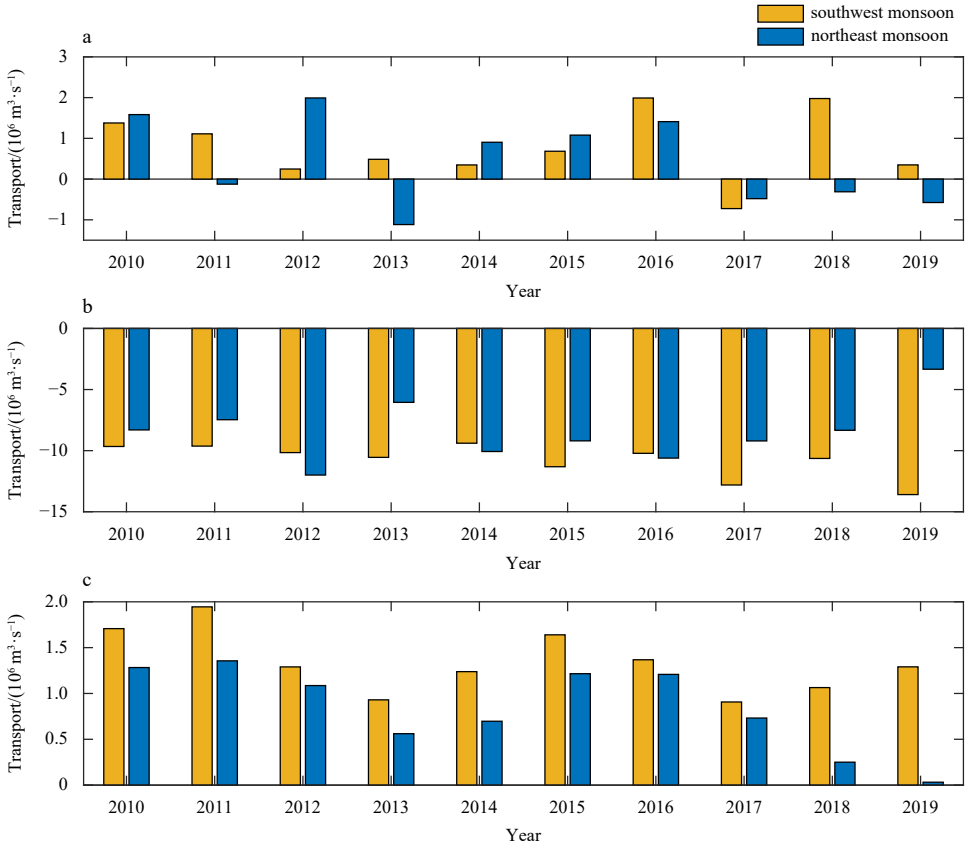

Fig. 13. Mean transport of the Preparis Channel (a), the Ten Degree Channel (b), and the Great Channel (c) during southwest monsoon and northeast monsoon periods during 2010 to 2019, based on ROMS output.

Table 1. The average transport and standard deviation for the three main channels (the Preparis Channel (PC), the Ten Degree Channel (TDC), and the Great Channel (GC)) during winter, spring, summer, autumn, southwest monsoon (SW), northeast monsoon (NE), and annual

Channel	Average transport and standard deviation/(10^6 m^3·s^{-1})						
	Winter	Spring	Summer	Autumn	SW	NE	Annual
PC	0.83 ± 0.86	1.49 ± 1.00	1.22 ± 1.11	1.01 ± 1.02	0.78 ± 0.84	0.44 ± 1.08	1.14 ± 0.43
TDC	−8.14 ± 2.90	−9.18 ± 3.00	−9.02 ± 4.13	−7.37 ± 4.96	−10.80 ± 1.40	−8.46 ± 2.45	−8.31 ± 1.26
GC	3.24 ± 3.76	3.78 ± 3.54	3.64 ± 3.26	3.52 ± 1.93	1.34 ± 0.34	0.84 ± 0.46	3.63 ± 1.24

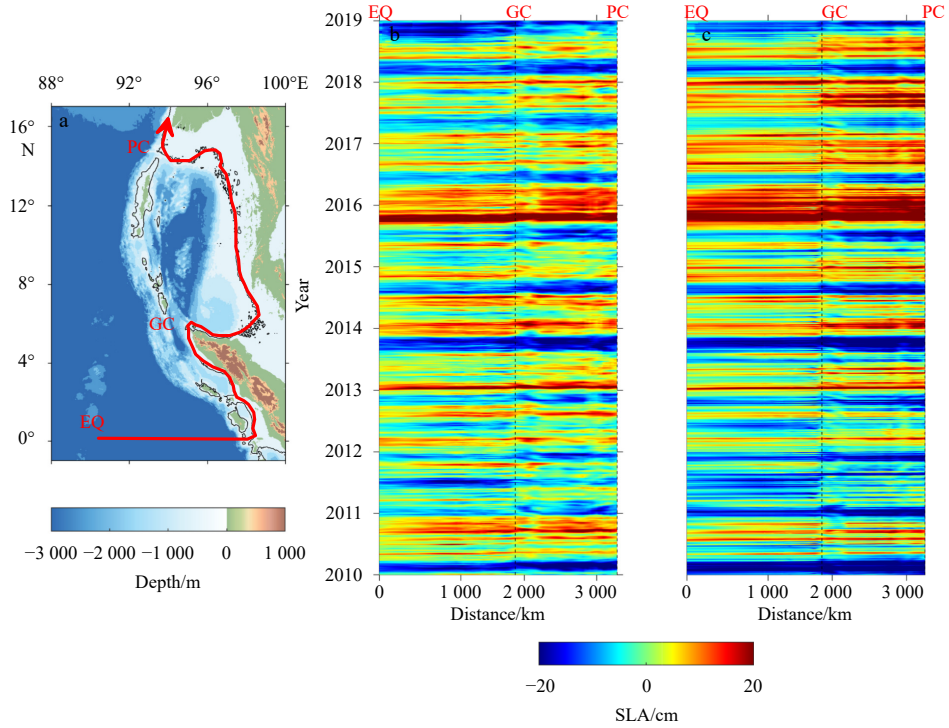

Fig. 14. Selected kelvin waves path along the 100-m depth contour of the Bay of Bengal (a), time-longitude plots of sea level anomaly (SLA) from Sea Level Thematic Assembly Centre (b), and Regional Ocean Modeling Systems model output (c). EQ, equator at 90°E; PC, Preparis Channel; GC, Great Channel.

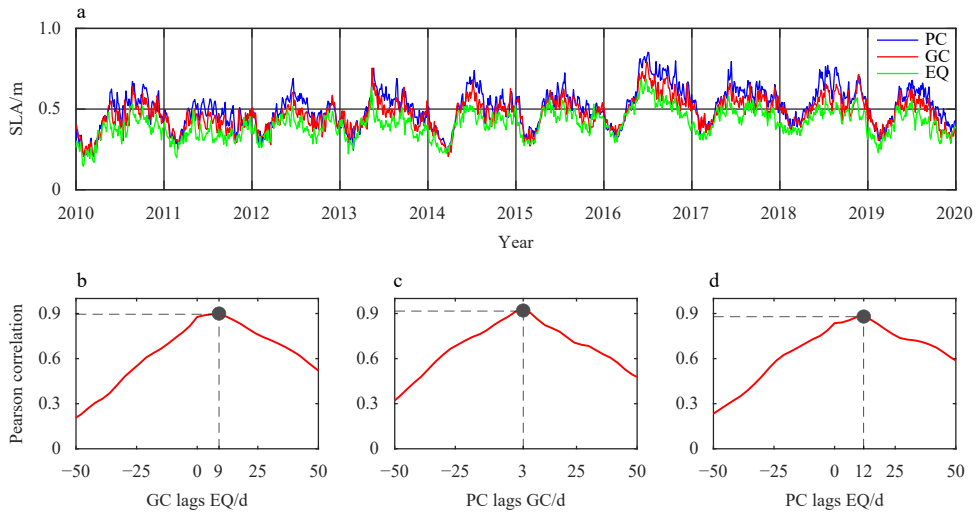

Fig. 15. The time series of sea level anomaly (SLA) for the Preparis Channel (PC), Great Channel (GC), and equator at 90°E (EQ) (a), and Pearson correlation of SLA between the EQ, GC, and PC (b, c, and d). The dots in b–d represent the number of days behind when the correlation is the strongest.

GC by 3 d, and the PC lags the EQ by 12 d, with corresponding mean correlation values around 0.9. This confirms the previous research on the Kelvin waves propagation pathway, indicating that the EQ, GC, and PC are indeed connected sequentially along the path of the equatorial Kelvin waves. That is, the equatorial Kelvin waves enter the AS through the GC before flowing out of the AS via the PC. Additionally, power spectral analysis of three time series shows significant semiannual variation at all three locations (Fig. 16).

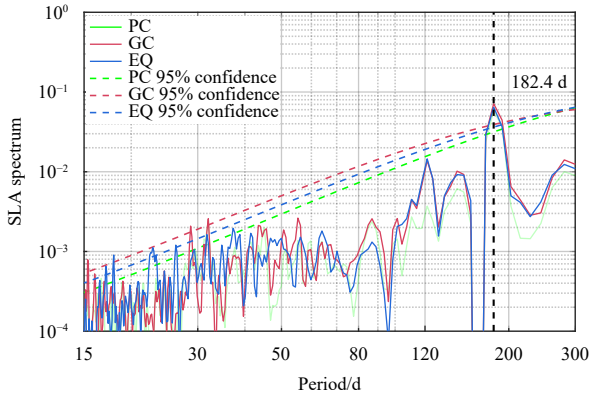

Fig. 16. Power spectral analysis of the time series of sea level anomaly (SLA). The dashed green, red, and blue lines show the 95% significance interval.

Therefore, we assert that during the monsoon transition period, equatorial zonal winds induce Kelvin waves that traverse the AS. In this process, semiannual Kelvin waves influence the sea surface height and flow fields within the AS, impacting the temporal variability of the upper level water exchange in the AS (Cheng et al., 2017). While the coastal propagation of Kelvin waves doesn't directly affect the TDC, the reflected waves from them radiate as Rossby wave packets and influence the local eddies and coastal circulations when blocked by islands, ultimately affecting the temporal variability of the TDC flow field (Chatterjee et al., 2017).

5 Discussion and summary

Based on the validated outputs from the ROMS numerical model for the period spanning from 2010 to 2019, we conducted a comprehensive study on the spatiotemporal characteristics of the water exchange transports in the three major channels of the AS.

The first EOF mode for the flow field in the PC channel indicates a division at approximately 100 m in depth, possibly associated with underwater topography. The TDC's first EOF mode shows relatively stable inflow into the AS, with strong seasonal oscillations in its corresponding principal component, which may be affected by the local forcing of coastal circulation (Chatterjee et al., 2017). Conversely, the GC's first EOF mode exhibits well-stratified water layers with consistent surface inflow, which may be related to the eastward surface flow in the equatorial Indian Ocean (Chen, 2022). Model results also suggest a possible multi-layer water exchange in the deep layer of the GC, like the PC and the Luzon Strait (Ye et al., 2023a; Cai et al., 2023). However, due to limitations in observational data for the GC, the actual conditions of the deep-sea flow warrant validation through measured data.

The locations with the most significant changes in transport per unit depth in all three channels are primarily in the surface layer and at depths of 100 m to 200 m, displaying seasonal variations. Semiannual variation emerges as a common feature in the transports of all three channels. This variation is also evident in their second principal component. The PC and the GC's average net transports are opposite in sign to the TDC's. When examining the linear trend, the sum of the PC and the GC's net transport linear regression coefficient is roughly equal in magnitude but opposite in sign to the TDC's. This suggests that the PC and the GC serve as the primary inflow channels into the AS, while the TDC serves as the primary outflow channel. Furthermore, during the northeast and southwest monsoons, the influence of these monsoons on the TDC and the GC appears to be more pronounced compared to the PC, likely due to the complex source of water passing through the PC. Vertical structure of transports and transport time series in all three channels reveal pronounced intraseasonal variations in the upper and middle layers, even after a 120-d low-pass filtering. Power spectral analysis indicates that all three channels exhibit a shared 182.4-d semiannual cycle and strong 15-d to 90-d intraseasonal oscillations, which underscores the significance of the semiannual variability as the dominant variability in water exchange transports in these channels. As for the intraseasonal variations within 90 d, MJO may be a contributing factor (Sharmila et al., 2013; Webber et al., 2014; Krishnamurti et al., 2017; Chen, 2022).

In the supplementary information, we validated the reliability of the ROMS model using satellite data and international datasets complementarily, and analyzed the transports in the Strait of Malacca. The Strait of Malacca, located in the eastern part of the AS and regulated by monsoons, serves as an important water exchange pathway with the South China Sea. It is characterized by a longer pathway and greater variability in water depth compared to the three channels examined in this paper, which may have implications for model performance. In the supplementary information, we analyzed the spatiotemporal variability of transports in the Strait of Malacca using two sections located at different distances from the AS, in Section 1 of the Strait of Malacca, the transport time series of the Strait of Malacca reveals a prominent semiannual cycle in the ten-year average transport of the Strait of Malacca, EOF analysis results demonstrate that the first principal component of cross-section velocity exhibits intraseasonal oscillations, and the second principal component shows a distinct semiannual cycle, similar to the other three channels. However, the semiannual variability does not reach the confidence line in Section 2 of the Strait of Malacca, suggesting a weaker influence of Kelvin waves compared to Section 1 of the Strait of Malacca, which is closer to the AS. We found that as we move further eastward along the Strait of Malacca, the strength of the semiannual periodic signal weakens. This suggests that coastal Kelvin waves entering the AS may also impact the spatiotemporal variability of the Strait of Malacca entrance, but their influence on the eastern part of the Strait of Malacca is relatively minor. Therefore, it should be distinguished from the other three channels that have comparatively shorter waterway distances. The model results successfully capture the spatiotemporal variability of water transport of the Strait of Malacca, except for some deviations in magnitude due to the selection of cross sections, coastal boundaries and complex topography, and the contributions of the Strait of Malacca to the AS will be furtherly evaluated in our future work.

Further investigation into the sea surface height propagation pathways reveals that during the monsoon seasons, equatorial zonal winds induce eastward-propagating semiannual Kelvin waves, which subsequently affect the sea surface height between the channels with discernible phase lags, ultimately impacting the flow fields in the AS.

In the supplementary information, However, it's important to

note that the results presented here are primarily based on model simulations, and further validation through field observations is warranted.

Acknowledgements

The authors thank the crew of R/V *Xiangyanghong 06* and R/V *Xiangyanghong 10* for their considerable assistance in the observation.

References

Amol P, Jain V, Aparna S G. 2022. Blue-shifted deep ocean currents in the equatorial Indian Ocean. Climate Dynamics, 59(1/2): 219–229, doi: 10.1007/s00382-021-06125-9

Amol P, Shankar D, Fernando V, et al. 2014. Observed intraseasonal and seasonal variability of the West India Coastal Current on the continental slope. Journal of Earth System Science, 123(5): 1045–1074, doi: 10.1007/s12040-014-0449-5

Bonjean F, Lagerloef G S E. 2002. Diagnostic model and analysis of the surface currents in the tropical Pacific Ocean. Journal of Physical Oceanography, 32(10): 2938–2954, doi: 10.1175/1520-0485(2002)032<2938:DMAAOT>2.0.CO;2

Cai Zhongya, Chen Dake, Gan Jianping. 2023. Formation of the layered circulation in South China Sea with the mixing stimulated exchanging current through Luzon Strait. Journal of Geophysical Research: Oceans, 128(3): e2023JC019730, doi: 10.1029/2023JC019730

Chatterjee A, Shankar D, McCreary J P, et al. 2017. Dynamics of Andaman Sea circulation and its role in connecting the equatorial Indian Ocean to the Bay of Bengal. Journal of Geophysical Research: Oceans, 122(4): 3200–3218, doi: 10.1002/2016JC012300

Chen Gengxin. 2022. The ocean wave bridge linking the circulation in the tropical eastern Indian Ocean. Advances in Earth Science (in Chinese), 37(1): 80–86

Chen Guosen, Wang Bin. 2021. Diversity of the boreal summer intraseasonal oscillation. Journal of Geophysical Research: Atmospheres, 126(8): e2020JD034137, doi: 10.1029/2020JD034137

Cheng Xuhua, McCreary J P, Qiu Bo, et al. 2017. Intraseasonal-to-semiannual variability of sea-surface height in the astern, equatorial Indian Ocean and southern Bay of Bengal. Journal of Geophysical Research: Oceans, 122(5): 4051–4067, doi: 10.1002/2016JC012662

Clarke A J, Liu X. 1993. Observations and dynamics of semiannual and annual sea levels near the eastern equatorial Indian Ocean boundary. Journal of Physical Oceanography, 23(2): 386–399, doi: 10.1175/1520-0485(1993)023<0386:OADOSA>2.0.CO;2

Du Ping, Zeng Dingyong, Lin Feilong, et al. 2023. Epipelagic mesozooplankton communities in the northeastern Indian Ocean off Myanmar during the winter monsoon. Acta Oceanologica Sinica, 42(6): 57–69, doi: 10.1007/s13131-022-2090-5

E. U. Copernicus Marine Service Information. 2023. Global ocean gridded L 4 sea surface heights and derived variables reprocessed 1993 ongoing. Marine Data Store (MDS). https://data.marine.copernicus.eu/product/SEALEVEL_GLO_PHY_L4_MY_008_047/description [2023-04-27/2024-01-05], doi: 10.48670/moi-00148

Eigenheer A, Quadfasel D. 2000. Seasonal variability of the Bay of Bengal circulation inferred from TOPEX/Poseidon altimetry. Journal of Geophysical Research: Oceans, 105(C2): 3243–3252, doi: 10.1029/1999JC900291

Evensen G. 2003. The ensemble Kalman filter: theoretical formulation and practical implementation. Ocean Dynamics, 53(4): 343–367, doi: 10.1007/s10236-003-0036-9

Fairall C W, Bradley E F, Hare J E, et al. 2003. Bulk parameterization of air-sea fluxes: Updates and verification for the COARE algorithm. Journal of Climate, 16(4): 571–591, doi: 10.1175/1520-0442(2003)016<0571:BPOASF>2.0.CO;2

Girishkumar M S, Ravichandran M, McPhaden M J, et al. 2011. Intraseasonal variability in barrier layer thickness in the south central Bay of Bengal. Journal of Geophysical Research: Oceans, 116(C3): C03009

Guo Ruoyu, Ma Xiao, Zhang Jingjing et al. 2022. Microbial community structures and important taxa across oxygen gradients in the Andaman Sea and eastern Bay of Bengal epipelagic waters. Frontiers in Microbiology, 13: 1041521, doi: 10.3389/fmicb.2022.1041521

Han Weiqing, Lawrence D M, Webster P J. 2001. Dynamical response of equatorial Indian Ocean to intraseasonal winds: zonal flow. Geophysical Research Letters, 28(22): 4215–4218, doi: 10.1029/2001GL013701

Huang Ke, McPhaden M J, Wang Dongxiao, et al. 2018. Vertical propagation of middepth zonal currents associated with surface wind forcing in the equatorial Indian Ocean. Journal of Geophysical Research: Oceans, 123(10): 7290–7307, doi: 10.1029/2018JC013977

Huang Ting, Zhou Feng, Tian Di, et al. 2020. Seasonal variations of mesoscale eddy in the Bay of Bengal and its adjacent regions. Journal of Marine Sciences, 38(3): 21–30, doi: 10.3969/j.issn.1001-909X.2020.03.003

Iskandar I, McPhaden M J. 2011. Dynamics of wind-forced intraseasonal zonal current variations in the equatorial Indian Ocean. Journal of Geophysical Research: Oceans, 116(C6): C06019

Ji Qiyan, Zhu Xueming, Wang Hui, et al. 2015. Assimilating operational SST and sea ice analysis data into an operational circulation model for the coastal seas of China. Acta Oceanologica Sinica, 34(7): 54–64, doi: 10.1007/s13131-015-0691-y

Johnson E S, Bonjean F, Lagerloef G S E, et al. 2007. Validation and error analysis of OSCAR sea surface currents. Journal of Atmospheric and Oceanic Technology, 24(4): 688–701, doi: 10.1175/JTECH1971.1

Kourafalou V H, De Mey P, Le Hénaff M, et al. 2015. Coastal Ocean Forecasting: system integration and evaluation. Journal of Operational Oceanography, 8(S1): s127–s146

Krishnamurti T N, Jana S, Krishnamurti R, et al. 2017. Monsoonal intraseasonal oscillations in the ocean heat content over the surface layers of the Bay of Bengal. Journal of Marine Systems, 167: 19–32, doi: 10.1016/j.jmarsys.2016.11.002

Liao Jiawen, Peng Shiqiu, Wen Xixi. 2020. On the heat budget and water mass exchange in the Andaman Sea. Acta Oceanologica Sinica, 39(7): 32–41, doi: 10.1007/s13131-019-1627-8

Lin Feilong, Liang Chujin, Ding Tao, et al. 2023. A preliminary study of suspended matters variation associated with hypoxia and shoaling internal tides on the continental shelf of the northern Andaman Sea. Journal of Marine Science and Engineering, 11(10): 1950, doi: 10.3390/jmse11101950

McCreary J P Jr, Kundu P K, Molinari R L. 1993. A numerical investigation of dynamics, thermodynamics and mixed-layer processes in the Indian Ocean. Progress in Oceanography, 31(3): 181–244, doi: 10.1016/0079-6611(93)90002-U

McPhaden M J. 1982. Variability in the central equatorial Indian Ocean Part I: Ocean dynamics. Journal of Marine Research, 40(1): 157–176

McPhaden M J, Meyers G, Ando K, et al. 2009. RAMA: the research moored array for African–Asian–Australian monsoon analysis and prediction. Bulletin of the American Meteorological Society, 90(4): 459–480, doi: 10.1175/2008BAMS2608.1

Mo Dongxue, Hou Yijun, Li Jian, et al. 2016. Study on the storm surges induced by cold waves in the northern East China Sea. Journal of Marine Systems, 160: 26–39, doi: 10.1016/j.jmarsys.2016.04.002

Mukherjee A, Shankar D, Fernando V, et al. 2014. Observed seasonal and intraseasonal variability of the East India Coastal Current on the continental slope. Journal of Earth System Science, 123(6): 1197–1232, doi: 10.1007/s12040-014-0471-7

Nagura M, McPhaden M J. 2012. The dynamics of wind-driven intraseasonal variability in the equatorial Indian Ocean. Journal of Geophysical Research: Oceans, 117(C2): C02001

Pargaonkar S M, Vinayachandran P N. 2022. The Irrawaddy river jet in the Andaman Sea during the summer monsoon. Frontiers in Marine Science, 9: 849179, doi: 10.3389/fmars.2022.849179

Pujiana K, McPhaden M J. 2020. Intraseasonal Kelvin waves in the

equatorial Indian Ocean and their propagation into the Indonesian seas. Journal of Geophysical Research: Oceans, 125(5): e2019JC015839, doi: 10.1029/2019JC015839

Rao R R, Kumar M S G, Ravichandran M, et al. 2010. Interannual variability of Kelvin wave propagation in the wave guides of the equatorial Indian Ocean, the coastal Bay of Bengal and the southeastern Arabian Sea during 1993–2006. Deep Sea Research Part I: Oceanographic Research Papers, 57(1): 1–13, doi: 10.1016/j.dsr.2009.10.008

Roman-Stork H L, Subrahmanyam B, Trott C B. 2020. Monitoring intraseasonal oscillations in the Indian Ocean using satellite observations. Journal of Geophysical Research: Oceans, 125(2): e2019JC015891, doi: 10.1029/2019JC015891

Saha S, Moorthi S, Pan Hualu, et al. 2010. The NCEP climate forecast system reanalysis. Bulletin of the American Meteorological Society, 91(8): 1015–1058, doi: 10.1175/2010BAMS3001.1

Sengupta D, Senan R, Goswami B N, et al. 2007. Intraseasonal variability of equatorial Indian Ocean zonal currents. Journal of Climate, 20(13): 3036–3055, doi: 10.1175/JCLI4166.1

Sengupta D, Senan R, Goswami B Nath. 2001. Origin of intraseasonal variability of circulation in the tropical central Indian Ocean. Geophysical Research Letters, 28(7): 1267–1270, doi: 10.1029/2000GL012251

Sengupta D, Senan R, Murty V S N, et al. 2004. A biweekly mode in the equatorial Indian Ocean. Journal of Geophysical Research: Oceans, 109(C10): C10003

Sharmila S, Pillai P A, Joseph S, et al. 2013. Role of ocean-atmosphere interaction on northward propagation of Indian summer monsoon intra-seasonal oscillations (MISO). Climate Dynamics, 41(5/6): 1651–1669

Shchepetkin A F, McWilliams J C. 2005. The regional oceanic modeling system (ROMS): a split-explicit, free-surface, topography-following-coordinate oceanic model. Ocean Modelling, 9(4): 347–404, doi: 10.1016/j.ocemod.2004.08.002

Shi Zhen, Li Xiang, Liu Na. 2016. Effects of different temporal resolution of wind and thermal forcing on simulated global ocean temperature. Marine Forecasts (in Chinese), 33(6): 1–9

Somayajulu Y K, Murty V S N, Sarma Y V B. 2003. Seasonal and interannual variability of surface circulation in the Bay of Bengal from TOPEX/Poseidon altimetry. Deep-Sea Research Part II: Topical Studies in Oceanography, 50(5): 867–880, doi: 10.1016/S0967-0645(02)00610-0

Trott C B, Subrahmanyam B. 2019. Detection of intraseasonal oscillations in the Bay of Bengal using altimetry. Atmospheric Science Letters, 20(7): e920, doi: 10.1002/asl.920

Varkey M J, Murty V S N, Suryanarayana A. 1996. Physical oceanography of the Bay of Bengal and Andaman sea. Oceanography and Marine Biology: An Annual Review, 34: 1–70

Vialard J, Shenoi S S C, McCreary J P, et al. 2009. Intraseasonal response of the northern Indian Ocean coastal waveguide to the Madden-Julian Oscillation. Geophysical Research Letters, 36(14): L14606

Wang Weiqiang, Zhu Xiuhua, Wang Chunzai, et al. 2014. Deep meridional overturning circulation in the Indian Ocean and its relation to Indian Ocean Dipole. Journal of Climate, 27(12): 4508–4520, doi: 10.1175/JCLI-D-13-00472.1

Webber B G M, Matthews A J, Heywood K J, et al. 2014. Seaglider observations of equatorial Indian Ocean Rossby waves associated with the Madden-Julian Oscillation. Journal of Geophysical Research: Oceans, 119(6): 3714–3731, doi: 10.1002/2013JC009657

Ye Ruijie, Zhou Feng, Ma Xiao, et al. 2023a. Observed characteristics of flow, water mass, and turbulent mixing in the Preparis Channel. Acta Oceanologica Sinica, 42(2): 83–93, doi: 10.1007/s13131-022-2021-5

Ye Ruijie, Zhou Feng, Ma Xiao, et al. 2023b. Energetic bottom current at the equatorial gap of the Ninety East Ridge in the Indian Ocean based on mooring data. Journal of Geophysical Research: Oceans, 128(3): e2022JC018974, doi: 10.1029/2022JC018974

Yoneyama K, Zhang Chidong, Long C N. 2013. Tracking pulses of the Madden-Julian Oscillation. Bulletin of the American Meteorological Society, 94(12): 1871–1891, doi: 10.1175/BAMS-D-12-00157.1

Zhang Chidong. 2005. Madden-Julian Oscillation. Reviews of Geophysics, 43(2): RG2003

Zhang Jiaying, Zhou Feng, Tian Di, et al. 2021. The characteristics and formation mechanism of the oceanic mesoscale eddy origin in northwest of Sumatra. Journal of Marine Sciences, 39(3): 1–11, doi: 10.3969/j.issn.1001-909X.2021.03.001

Zhou Xiwu, Qiu Yun, Lin Xinyu, et al. 2022. An intrathermocline eddy observed in the northeastern Bay of Bengal. Geophysical Research Letters, 49(12): e2022GL099201, doi: 10.1029/2022GL099201

Zhu Xueming, Zu Ziqing, Ren Shihe, et al. 2022. The improvements to the regional South China Sea operational oceanography forecasting system. Geoscientific Model Development Discussions, 15(3): 995–1015, doi: 10.5194/os-2020-104

Supplementary information:

Fig. S1. 10-year average seasonally surface temperature in winner (a, e), spring (b, f), summer (c, g), and autumn (d, h) in the Andaman Sea during 2010–2019, based on OSTIA data (a–d) and ROMS (e–h).

Fig. S2. 10-year average seasonal surface salinity in winner (a, e), spring (b, f), summer (c, g), and autumn (d, h) in the Andaman Sea during 2010–2019, based on SMOS data (a–d) and ROMS (e–h).

Fig. S3. Topography of the Preparis Channel including the JAMES cruise CTD stations selected for temperature and salinity profiles comparison with ROMS.

Fig. S4. Statistical comparison of temperature and salinity between CTD profiles and ROMS profiles.

Fig. S5. Topography of the Andaman Sea including the cross section of the Bay of Bengal at 10°N and the cross section of the Andaman Sea at 10°N.

Fig. S6. Cross section distributions of 10-year averaged temperature (℃, top) and salinity (bottom) between ROMS (a, c) and WOA dataset (b, d) along 10°N, respectively.

Fig. S7. Temperature and salinity profiles averaged from WOA dataset and ROMS data in the Bay of Bengal (10°N, 90°E to 93°E) and the Andaman Sea (10°N, 93°E to 96°E) respectively.

Fig. S8. Statistical comparison of 10-year averaged temperature and salinity profiles at 10°N between WOA dataset and ROMS in the Bay of Bengal (a and b) and the Andaman Sea (c and d).

Fig. S9. The climatological monthly variability of water transport at Section 1 of the Strait of Malacca based on the HYCOM, ROMS and SODA during 2010–2019.

Fig. S10. Bathymetry (m) of the Strait of Malacca with two sections for transport calculation.

Fig. S11. Time series and trends of transport at the Section 1 of the Malacca Strait based on ROMS output (a) and the power spec-

tra of full depth water transport in three channels based on unfiltered ROMS data (b).

Fig. S12. Time series and trends of transport at the Section 2 of the Malacca Strait based on ROMS output (a) and the power spectra of full depth water transport in three channels based on unfiltered ROMS data (b).

Fig. S13. Vertical section for the Section 1 of the Malacca Strait.

Fig. S14. The EOF modes for the Section 1 of the Malacca Strait (a and b). The first principal component (PC1), the second principal component time series (PC2) and their power spectrum corresponding to the Malacca Strait (c, d, and e).

Fig. S15. Vertical section for the Section 2 of the Malacca Strait.

Fig. S16. The EOF modes for the Section 2 of the Malacca Strait (a and b). The first principal component (PC1), the second principal component time series (PC2) and their power spectrum corresponding to the Malacca Strait (c, d, and e).

Table S1. 10-year average seasonal RMSE and R^2 Comparison for OSTIA and SMOS dataset Against ROMS validation during winter, spring, summer, and autumn.

Table S2. Multi-year average transports and standard deviations (unit: 10^6 m^3/s) across two sections for the three datasets.

The supplementary information is available online at https://doi.org/10.1007/s13131-024-2317-8 and http://www.aosocean.com/. The supplementary information is published as submitted, without typesetting or editing. The responsibility for scientific accuracy and content remains entirely with the authors.